Supplemental Material for Ultrafast modification of the electronic structure of a correlated insulator

O. Grånäs,[1] I. Vaskivskyi,[1, 2] X. Wang,[1] P. Thunström,[1] S. Ghimire,[3] R. Knut,[1] X. Wang,[1] J. Söderström,[1] L. Kjellsson,[1] D. Turenne,[1] R. Y. Engel,[4] M. Beye,[4] J. Lu,[3] D. J. Higley,[5] A. H. Reid,[5] W. Schlotter,[5] G. Coslovich,[5] M. Hoffmann,[5] G. Kolesov,[6] C. Schüßler-Langeheine,[7] A. Styervoyedov,[8] N. Tancogne-Dejean,[9] M. A. Sentef,[9] D. A. Reis,[3] A. Rubio,[9, 10] S. S. P. Parkin,[8] O. Karis,[1] J.-E. Rubensson,[1] O. Eriksson,[1, 11] and H. A. Dürr[1]

[1]*Department of Physics and Astronomy, Uppsala University, Uppsala, Sweden* *
[2]*Center for Memory and Recording Research, University of California San Diego,*
9500 Gilman Drive, La Jolla, CA 92093-0401, USA
[3]*Stanford PULSE Institute, SLAC National Accelerator Laboratory,*
2575 Sand Hill Road, Menlo Park, CA 94025, USA
[4]*Department of Photon Science, DESY, Notkestraße 85, D-22607 Hamburg, Germany*
[5]*SLAC National Accelerator Laboratory, 2575 Sand Hill Road, Menlo Park, CA 94025, USA*
[6]*John Paulson School of Engineering and Applied Sciences,*
Harvard University, Cambridge, Massachusetts 02138, USA
[7]*Helmholtz-Zentrum Berlin für Materialien und Energie GmbH, 12489 Berlin, Germany*
[8]*Max-Planck Institut für Mikrostrukturphysik, Weinberg 2, Halle, Germany*
[9]*Max Planck Institute for the Structure and Dynamics of Matter and Center for Free-Electron Laser Science,*
Luruper Chaussee 149, 22761 Hamburg, Germany
[10]*Center for Computational Quantum Physics, Flatiron Institute, New York, NY 10010 USA*
[11]*School of Science and Technology, Örebro University, SE-701 82, Örebro, Sweden*
(Dated: July 4, 2022)

I. EXPERIMENTAL METHODS

A. Sample growth

The NiO layers used in the experiments were grown on double polished MgO(001) substrates. Polishing both front and back sides of the MgO substrate ensured that the XAS samples could also be used for HHG experiments. A 2 nm thick MgO underlayer was deposited by RF magnetron sputtering in 3 mTorr argon at a temperature below 100 C followed by a NiO layer that was deposited at 700 °C in an Ar(90%)/O2(10%) gas mixture at a pressure of 3 mTorr and was then annealed in-situ at the same temperature (700 °C) for 15 min in the same Ar-O2 gas mixture. In addition, 30 nm thin NiO transmission films were used for tuning the x-ray energy when setting up the experiment. They were grown by molecular beam epitaxy on 200 nm Si3N4 membranes. Ni metal was evaporated in an oxygen atmosphere of 3.10-7 mbar, the substrate was held at 250 C, the growth rate was 1.8 Å/min.

B. Optical characterization

In order to evaluate the amount of energy that was deposited in the NiO film during the optical excitation process, we measured the optical absorption of our sample between 500 nm and $2\mu m$, and evaluated the absorption coefficient of the NiO film that was used in the time-resolved x-ray absorption measurement.

Figure S1a shows both the measured absorption and the calculated absorption using tabulated absorption coefficient and magnified absorption coefficient. In the experimental data, there are two absorption bands centered around 0.7 μm and 1.2 μm, which have been assigned as the intra d-d transitions [3, 4]. In Figure S1a, one can see that the calculated absorption using the tabulated absorption coefficient, shown as the dashed curves, has lower amplitude than the experimental data across the whole range. In order to match the absorption amplitude in the experimental data, we multiplied the tabulated absorption coefficient with a constant and calculated the absorption based on the magnified absorption coefficient. By adjusting the multiplication constant, we could get good match for the amplitude at the two absorption bands, as represented by the solid curves in Figure S1a.
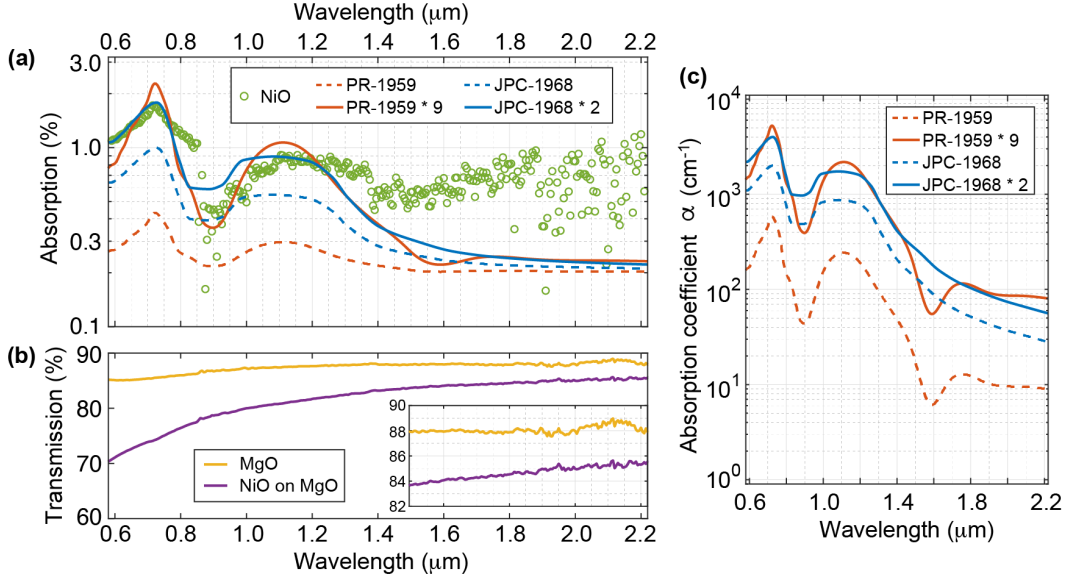
---

* oscar.granas@physics.uu.se

FIG. S1. (a) Optical absorption of the NiO film within the range [0.5 μm, 2.5 μm]. The symbols represent the measured optical absorption. The dashed curves represent the calculated absorption using the absorption coefficient α directly from Refs. [1, 2]. The solid curves represent the calculated absorption using magnified absorption coefficient from Refs. [1, 2]. (b) The optical transmission of the MgO substrate and the sample (NiO grown on MgO). (c) The absorption coefficients α that are used in the calculation of absorption shown in (a).

It is noticeable that there is discrepancy between the measured absorption and the calculated absorption at long wavelengths ($\lambda > 1.5$ μm). This discrepancy arises from the normalization with the substrate. In the optical measurements, both the transmission and the reflection of the sample (NiO on MgO) were measured. In order to get the transmission of the NiO film, the transmission of the sample was normalized by the transmission of the substrate (MgO). Figure S1b shows the measured transmission of the sample and the substrate. The inset shows the zoom-in ordinate scale for wavelengths $\lambda > 1.5$ μm. The transmission of the substrate is higher at longer wavelengths than shorter wavelengths, which leads to under-estimation in the transmission of the NiO film. The absorption of the NiO film was calculated by subtracting the transmission and reflection from the unity. Therefore, the under-estimation of the transmission will cause the over-estimation of the absorption, which explains the discrepancy between the experimental data and calculation at long wavelengths. Earlier published absorption spectrum [5], has shown the absorption stayed at low level for wavelengths > 1.5 μm.

Figure S1c shows the absorption coefficient α that is used for the calculation of absorption shown in Figure S1a. We read the absorption coefficient from the solid curves (74 cm-1 and 86 cm^{-1}) and use the average value (80 cm^{-1}) as the absorption coefficient of the NiO film. The refractive index of NiO at 2 μm is 2.02 [6], and the reflection is 10

C. X-ray Absorption Spectroscopy measurements on NiO

The XAS spectra were measured at the SXR instrument of the Linac Coherent Light Source (LCLS) at SLAC National Accelerator Laboratory in Stanford/USA. The X-ray pulses with linear horizontal polarization were focused by a pair of Kirkpatrick-Baez mirrors and impinged on the sample at 70° with respect to surface resulting in an elliptical beam footprint of 400x80 µm^2. The pulse energy for 50 fs x-ray pulses was set to about 0.3 μJ and 2 μJ at oxygen and nickel edge respectively. This results in values of the x-ray fluence of $0.1 - 0.15$ mJ/cm^2 (O 1s-2p resonance) and 0.65-0.85 mJ/cm^2 (Ni 2p-3d resonance) on the sample. The spectra were recorded in the x-ray energy ranges of 533-538 eV and 849-861 eV for O 1s-2p and Ni 2p-3d core-valence resonances, respectively. XAS was detected in fluorescence yield mode with large area microchannel plates insensitive to the pump laser photons. The pump laser with the central wavelength of 2 μm (0.6 eV photon energy) and linear horizontal polarisation from a synchronized femtosecond laser source was coupled collinearly to the x-ray beam. To ensure homogeneous excitation of the probed spot the pump spot size was set to 1 mm. LCLS operations allowed us to move repeatedly between edges to corroborate consistency between O K- and Ni L- edge measurements, the pump-probe overlap was also repeatedly checked. To ensure that spectral bleaching, known to occur due to the XAS process [4], is not affecting

our measurements, each pump-probe cycle probes a new spot. We optically characterize the sample before and after measurements to ensure all changes are reversible and the sample is not altered by the pump-probe process, see supplemental material section I.B for details.

Time-delay traces (Fig. 1c) were measured at two fixed photon energies in the pre-edge regions of O and Ni absorption bands. The rise-time of the signal in Fig. 1, as well as overall time-resolution in the experiment was mainly limited by the duration of the pump pulse (150 fs). To measure the spectra for the two different pump polarizations (E || [100] and E || [110] in Fig. 2b) the sample was rotated by 45°, while keeping the polarization of the pump and probe beams unchanged. This ensured unchanged pump-probe overlap and spot size in both experiments and minimizes the differences due to optical reflections of the pump pulse from the sample. At the highest used pump fluence, permanent damage of the sample occurred after 2-5 min exposure. To avoid degradation of spectra, the sample was moved to a fresh spot every 90 s. The characteristics of the pump and probe pulses are determined so as the combined intensity is below the damage threshold of the sample. All measurements shown here were performed at room temperature, i.e. below the equilibrium NiO antiferromagnetic ordering Neel temperature of 525 K, which is determined largely by an exchange coupling of 18 meV [7].

D. Optical High-harmonics generation (HHG) in NiO

High-order harmonics (Fig. 2a) were measured in the transmission geometry at normal incidence, independently to the XAS measurements but in similar laser conditions. The light source was an optical parametric amplifier (OPA, HE-TOPAS-Prime, Light Conversion) pumped by a Ti:sapphire amplifier system (Legend Elite Duo, Coherent) operating at a 1 kHz repetition rate. The idler pulse at 2.08 μm in wavelength from the OPA was loosely focused onto the NiO side of the sample. The pulse duration is around 60 fs. The area of the focal spot on the sample surface was estimated to be 0.0297 cm^2 from a knife edge measurement. The pulse energy was set at 16 μJ. The high-harmonic beam propagating along the transmission direction was collected by a lens and focused into the entrance slit of a spectrometer, which consisted of a grating-based monochromator (Acton, VM-504, grating: 300 grooves mm^{-1}) and a charge-coupled device (CCD, Andor DO440). Spectrally resolved high-harmonic signals emerging from the NiO film were recorded by the CCD. A bare MgO substrate was tested under the same laser fluence and only third-harmonic signal was observed [8]. This confirms that the reported HHG signals all emerged from the NiO film. Because of the wider band-gap in MgO, it requires a higher fluence to produce high-harmonics that are detectable. Similarly, reported harmonics have photon energy below the bandgap of MgO substrate and therefore the substrate is transparent.

II. COMPUTATIONAL METHODS

A. Determination of optimal pump characteristics

In order to minimize the number of electrons that the pump-pulse excites to the conduction band, we tailor our pump pulse to minimize Zener-tunnelling and multi-photon transitions, and of course direct transitions. To achieve this goal, we use the so-called Keldysh-parameter, γ_k, relating materials- and pulse-properties to estimate the regime we are operating in. The dynamical Franz-Keldysh effect has previously been studied in wide band-gap semiconductors, with $\gamma_k \approx 3$ [9]. Studies exploring conditions for Zener-tunnelling are also available, indicating a lower bound in the range of $\gamma_k \approx 3$. We ensure our pulse is slightly above this lower bound. Additionally, we need to keep the combined pump- and probe-pulse intensity below the damage threshold, while still allowing us to probe both the O K- and Ni L-edges. The optical gap of NiO at room temperature is reported to be 3.4 eV-4.0 eV, the reduced effective carrier mass of NiO is m~1m$_\mathrm{e}$. With the conditions for γ_k in mind we experimentally use a maximum field amplitude and photon energy of E_0 =0.22 V/Å and ω_0 =0.6 eV, respectively. leading to $\gamma_k \approx 5$, a suitable range of ponderomotive energy in relation to materials characteristics [10, 11]. Of importance is also that the 0.6eV photon energy is far from any in-gap excitations, as determined by optical measurements where lowest three in-gap d-d absorptions lines are reported to be at 1.07 eV, 1.68 eV and 1.83 eV. The above mentioned characteristics is equivalent to a modification of the energy-landscape in the order of 30% of the bandwidth for electronic states extending over the lattice parameter in the material, or 7500% of the magnetic super-exchange coupling.

B. Model for a correlated insulator

While it is important to note that tight-binding models are always approximate in relation to a fully hybridizing first-principle description, valuable insights can often be deduced from models. Following Khomskii [12], we introduce

the Hamiltonian

$$H = \epsilon_d \sum_{i,\sigma} d_{i,\sigma}^\dagger d_{i,\sigma} + \epsilon_p \sum_{j,\sigma} p_{j,\sigma}^\dagger p_{j,\sigma} + \sum_{ij,\sigma\sigma'} (t_{(pd)ij} d^\dagger i, \sigma p_{j,\sigma'} + h.c.) \tag{1}$$

$$+ U_{dd} \sum_i n_{d_{i\uparrow}} n_{d_{i\downarrow}} + U_{pp} \sum_j n_{p_{j\uparrow}} n_{p_{j\downarrow}} + U_{pd} \sum_{ij,\sigma\sigma'} n_{d_{i\sigma}} n_{p_{j\sigma'}} \tag{2}$$

where the operators d and p refers to orbital holes in the d and p shell on Ni and O respectively. The effective Coulomb interaction U is defined for intra-shell dd and pp as well as inter-shell dp contributions. Spin is indexed by σ. The ability to hop between sites is governed by t_{pd}, that effectively also mediates hopping between Ni sites via oxygen. The charge-transfer parameter is defined as the difference in relative energy between an unperturbed d and p level $\Delta_{CT} = \epsilon_d - \epsilon_p$.

To relate the above model to the archetypal Hubbard-model, we note that the effective coulomb interaction is strongest between the d-electrons on the Ni site, while it is significantly weaker around the oxygen-atoms. To simplify the model one can then reduce the role of the oxygen orbitals to only provide a channel for the hopping between Ni-sites through an orbital down-folding procedure. This approximation reduces the model to just Ni-sites, with a renormalized effective hopping $t_{dd}^{\text{eff}} = \frac{t_{pd}^2}{\Delta_{CT}} \equiv t$, where Δ_{CT} is the charge-transfer energy and the relevant effective Coulomb interaction is $U_{dd} \equiv U$. The intra-cycle field-induced polarization of the oxygen p-states influences the t_{pd}-parameter, hence also the effective hopping t_{dd}^{eff}. This modification also influences the effective magnetic interaction between the antiferromagnetically aligned Ni-spins.[12]

Estimating effective hopping and interaction parameters for tight-binding models is highly non-trivial. In particular, the effective Coulomb interaction U, depends not only on the orbitals, but also on frequency. This frequency dependence originates in the screening-processes that covers a large spatial- and temporal range. These screening processes are affected by out-of-equilibrium conditions. This complexity renders a full many-body solution tractable for only a few states, and TD-DFT based first-principles methods approximate U to be either inert (slow change in screening processes on the scale of the dynamics probed) or instantaneous (fast change in screening processes on the scale of the dynamics probed). This is the main difference in the assumed dynamics of U between the current work and earlier predictions of a strong transient renormalization.[13]

To be more specific, the effective Coulomb interaction parameter $U_{eff}(t)$ was in Ref. 13 assumed to take the same approximate band structure-dependent form as in Ref. 14, but for the instantaneous Hamiltonian instead of the equilibrium Hamiltonian. The approximate screening factor of $U_{eff}(t)$ corresponds therefore to the integral of the *square* of the Ni 3d orbital character for each occupied band evaluated at time t.[14] Due to the square the screening depends on the Ni 3d orbital character of each individual band, which is particularly sensitive to the avoided crossings with other hybridizing bands. When the value of $U_{eff}(t)$ changes due to the screening, so does the effective Ni 3d potential and hence the avoided crossings, which can cause a feedback loop. A small perturbation to the lattice potential can therefore give rise to an unphysically large response in the approximate screening of $U_{eff}(t)$.

C.   First-principles calculations

Conventional first principles methods based on Kohn-Sham density-functional theory in the semi-local approximation, e.g. GGA [15] fails to reproduce many of the features of strongly correlated electron materials. Nickel oxide shows signatures of localized atomic-like states as well as band-like electronic states with significant dispersion. To account for the weakly screened Coulomb repulsion between electrons of d-character, an on-site term adopted from the Hubbard Hamiltonian, often denoted "Hubbard U", is included in the Hamiltonian. A U-value of 7-8 eV results in an appropriate band-gap of about 4 eV, which is an order of magnitude larger than that predicted by pure semi-local DFT. Our calculations aim to reproduce the behavior of NiO below the Néel temperature, and is thus anti-ferromagnetically ordered [16]. To support our experimental data and to interpret our results, we use the DFT+Hubbard U Hamiltonian to describe the system, according to the sub-sections below.

The XAS spectra of the Ni L-edge in Fig. 1e are obtained from a multi-configurational approach based on density-functional theory combined with multiplet ligand field theory [17, 18] for the Ni 3d states, using the parameters from Ref. [18]. The presence of the core-hole of the 2p shell and its non-trivial coupling to the valence electrons is explicitly included in the calculations, as implemented in a full-potential, linear muffin-tin orbitals method (RSPt) [19]. Figure 1c shows a qualitative estimate of how the XAS spectra are modified in the presence of a strong dynamical screening of U ($U \rightarrow \tilde{U}$). This was modelled by reducing the effective U from 6.9 eV to 6.2 eV, which also modifies the double counting correction from 100.2 eV to 94.6 eV. To estimate the effect of a modulated hopping term ($t \rightarrow \tilde{t}$) on the XAS of the O 1s-2p transitions, we performed calculations of NiO in the AFM ordered phase using the APW+lo software Elk [20]. The band-broadening was induced by compressing the lattice 1% from the equilibrium geometry. Further,
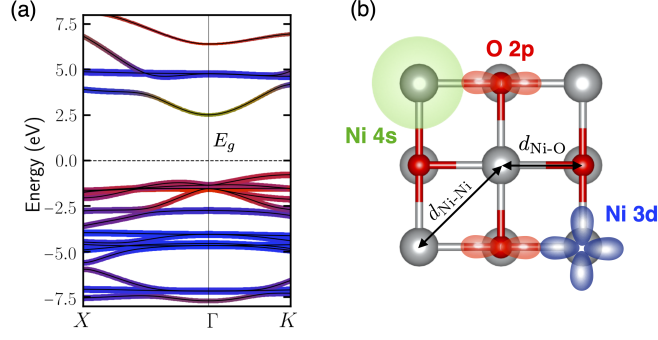
FIG. S2. (a) Band-structure of NiO along the $X - \Gamma - K$ cut in the Brillouin zone. The colors of the bands indicate orbital-projected band-character, blue for Ni 3d, green for Ni 4s, red for O 2p. The width of the band indicates the amount of projection that is in the close vicinity of an atom, i.e. a thin line indicates a large weight in the interstitial region. (b) Lattice structure depicting the real-space character of a sub-set of representative orbitals on which the band-structure in panel (a) is projected.

the maximum number of plane-waves to include in the basis was determined by setting the maximum $|G+k|$ RMT to 8, where RMT is the average radius of the augmentation muffin tins, G is a reciprocal lattice vector, and k a crystal momentum within the first Brillouin zone. The full Brillouin-zone was sampled by 123 k-points in order to perform integration in reciprocal space. Similar settings were used to calculate the band-structure and band-character of NiO in figure S2. The muffin-tin radius was varied in order to estimate the gradient of oxygen to nickel character on the interstitial states. We note that the spectra from the static situation (red curves, marked "ground state" in figure 1 a and b), are in good agreement with the theoretical data in figure 1d and e, both for the O 1s-2p and the Ni 2p-3d XAS. This level of agreement has been known from previous work [17, 18, 21].

D. Time-dependent density response and density of states

The implementation of time-dependent density-functional theory used to determine the transient changes in charge density and density of state, as shown in figure 3 of the main text, is based on an extension of the Siesta software [22], as described in Kolesov et al. [23]. Further, the vector potential and coupling to macroscopic fields are implemented according to Bertsch et al [24]. The external field is included in the Coulomb-gauge, as a vector potential of $A(t) = (E_0 \int_{t=0}^{t} \sin(\omega t')dt'$, where (E_0)=0.2 V/Åin the [100] direction, T = 6.9 fs and ω =0.6 eV. The basis set consists of numerical atom-centred double-Zeta + polarization orbitals. Grid integrals are performed on an equidistant mesh with a 120 Ry cut-off. The real-time propagation is performed in time-steps of 6.05 atto-seconds. The local magnetic moment and charge transfer is extracted from Mulliken charges associates with the atom-centred orbitals. Indicating that the majority of charge transfer is associated with O 2px and Ni 4s states. The time-evolved density of states is calculated as the sum of expectation values of the time-evolved wave-functions, i.e. $\epsilon_i(t) = \langle \psi_i(t)|H(t)|\psi_i(t)\rangle$, represented with a gaussian broadening of 0.3 eV. The exchange and correlation were treated within the generalized gradient + Hubbard U approximation (GGA+U) [15, 25]. The effective U is set to 7 eV, reproducing the experimental band-gap of 4 eV. In our calculation we keep the effective U fixed. When allowing for a dynamical response of U as an adiabatic functional of the density matrix (no retardation/memory effects in the functional), one sees pronounced changes of U and thus the electronic structure involving also bands of primarily Ni 3d-character. This is contrary to the experimental findings under the pump-characteristics we have considered here. This points in turn to the importance of developing the theory for real-time dynamics of strongly correlated materials further, beyond the adiabatic treatment of screening for first principles non-equilibrium dynamics [26].

Visualizations are made in Vesta [27], and using python/matplotlib [28].

[1] R. Newman and R. M. Chrenko, Optical Properties of Nickel Oxide, Phys Rev **114**, 1507 (1959).
[2] I. Austin, B. Clay, and C. Turner, Optical absorption of small polarons in semiconducting NiO and CoO in the near and far infra-red, Journal of Physics C: Solid State Physics **1**, 1418 (1968).
[3] T. Tsuboi and W. Kleemann, Fine structure of near infrared optical absorption in NiO, J Phys: Cond Mat **6**, 8625 (1994).
[4] V. I. Sokolov, V. A. Pustovarov, V. N. Churmanov, V. Y. Ivanov, N. B. Gruzdev, P. S. Sokolov, A. N. Baranov, and A. S.

Moskvin, Unusual x-ray excited luminescence spectra of NiO suggest self-trapping of the d-d charge-transfer exciton, Phys Rev B **86**, 115128 (2012).

[5] G. R. Rossman, R. D. Shannon, and R. K. Waring, Origin of the yellow color of complex nickel oxides, Journal of Solid State Chemistry **39**, 277 (1981).

[6] M. El-Nahass, M. Emam-Ismail, and M. El-Hagary, Structural, optical and dispersion energy parameters of nickel oxide nanocrystalline thin films prepared by electron beam deposition technique, Journal of Alloys and Compounds **646**, 937 (2015).

[7] M. T. Hutchings and E. J. Samuelsen, Measurement of spin-wave dispersion in NiO by inelastic neutron scattering and its relation to magnetic properties, Phys Rev B **6**, 3447 (1972).

[8] Y. S. You, D. A. Reis, and S. Ghimire, Anisotropic high-harmonic generation in bulk crystals, Nature Physics **13**, 345 (2016).

[9] M. Lucchini, S. A. Sato, A. Ludwig, J. Herrmann, M. Volkov, L. Kasmi, Y. Shinohara, K. Yabana, L. Gallmann, and U. Keller, Attosecond dynamical Franz-Keldysh effect in polycrystalline diamond, Science **353**, 916 (2016).

[10] S. Ghimire, A. D. DiChiara, E. Sistrunk, U. B. Szafruga, P. Agostini, L. F. DiMauro, and D. A. Reis, Redshift in the Optical Absorption of ZnO Single Crystals in the Presence of an Intense Midinfrared Laser Field, Phys Rev Lett **107**, 1307 (2011).

[11] S. Y. Kruchinin, F. Krausz, and V. S. Yakovlev, Colloquium: Strong-field phenomena in periodic systems, Rev Mod Phys **90**, 021002 (2018).

[12] D. I. Khomskii, *Transition Metal Compounds* (Cambridge University Press, 2014).

[13] N. Tancogne-Dejean, M. A. Sentef, and A. Rubio, Ultrafast Modification of Hubbard U in a Strongly Correlated Material: Ab initio High-Harmonic Generation in NiO, Phys Rev Lett **121**, 097402 (2018).

[14] L. A. Agapito, S. Curtarolo, and M. Buongiorno Nardelli, Reformulation of DFT + u as a pseudohybrid hubbard density functional for accelerated materials discovery, Phys. Rev. X **5**, 011006 (2015).

[15] J. P. Perdew, Generalized gradient approximation made simple, Phys Rev Lett **77**, 3865 (1996).

[16] W. L. Roth, Magnetic structures of MnO, FeO, CoO, and NiO, Phys Rev **110**, 1333 (1958).

[17] M. W. Haverkort, M. Zwierzycki, and O. K. Andersen, Multiplet ligand-field theory using Wannier orbitals, Phys Rev B **85**, 165113 (2012).

[18] J. Lüder, J. Schött, B. Brena, M. W. Haverkort, P. Thunström, O. Eriksson, B. Sanyal, I. Di Marco, and Y. O. Kvashnin, Theory of L-edge spectroscopy of strongly correlated systems, Phys Rev B **96**, 245131 (2017).

[19] J. M. Wills, O. Eriksson, P. Andersson, A. Delin, O. Grechnyev, and M. Alouani, *Full-Potential Electronic Structure Method, Energy and Force Calculations with Density Functional and Dynamical Mean Field Theory*, Energy and Force Calculations with Density Functional and Dynamical Mean Field Theory, Vol. 167 (Springer Berlin Heidelberg, Berlin, Heidelberg, 2010).

[20] J. K. Dewhurst, S. Sharma, L. Nordström, F. Cricchio, O. Grånäs, and E. K. U. Gross, *The Elk Code Manual* (2020).

[21] G. A. Sawatzky and J. W. Allen, Magnitude and Origin of the Band Gap in NiO, Phys Rev Lett **53**, 2339 (1984).

[22] J. M. Soler, E. Artacho, J. D. Gale, A. García, J. Junquera, P. Ordejón, and D. Sánchez-Portal, The SIESTA method for ab initio order-N materials simulation, J. Phys. Condens. Matter **14**, 2745 (2002).

[23] G. Kolesov, O. Grånäs, R. Hoyt, D. Vinichenko, and E. Kaxiras, Real-Time TD-DFT with Classical Ion Dynamics: Methodology and Applications, J Chem Theory Comput **12**, 466 (2016).

[24] G. F. Bertsch, J. I. Iwata, A. Rubio, and K. Yabana, Real-space, real-time method for the dielectric function, Phys Rev B **62**, 7998 (2000).

[25] S. L. Dudarev, G. Botton, S. Y. Savrasov, C. Humphreys, and A. Sutton, Electron-energy-loss spectra and the structural stability of nickel oxide: An LSDA+U study, Phys Rev B **57**, 1505 (1998).

[26] N. Tancogne-Dejean, M. A. Sentef, and A. Rubio, Ultrafast Transient Absorption Spectroscopy of the Charge-Transfer Insulator NiO: Beyond the Dynamical Franz-Keldysh Effect, Phys Rev B **102**, 115106 (2020).

[27] K. Momma and F. Izumi, VESTA: a three-dimensional visualization system for electronic and structural analysis, J Appl Crystallogr **41**, 653 (2008).

[28] J. D. Hunter, Matplotlib: A 2D Graphics Environment, Comput Sci Eng **9**, 90 (2007).